Monthly Notices of the ROYAL ASTRONOMICAL SOCIETY

MNRAS **470,** 4662–4670 (2017) doi:10.1093/mnras/stx1486

# The molecular environment of the pillar-like features in the H II region G46.5–0.2

S. Paron,[1,2]★ M. Celis Peña,[1] M. E. Ortega,[1] C. Fariña,[3,4] A. Petriella,[1] M. Rubio[5] and R. P. Ashley[3,6]

[1]*CONICET–Universidad de Buenos Aires, Instituto de Astronomía y Física del Espacio CC 67, Suc. 28, 1428 Buenos Aires, Argentina*
[2]*Universidad de Buenos Aires, Facultad de Arquitectura Diseño y Urbanismo, Buenos Aires, Argentina*
[3]*Isaac Newton Group of Telescopes, E38700 La Palma, Spain*
[4]*Instituto de Astrofísica de Canarias (IAC) and Universidad de La Laguna, Dpto. Astrofísica, La Laguna, Spain*
[5]*Departamento de Astronomía, Universidad de Chile, Casilla 36-D, Santiago, Chile*
[6]*Department of Physics, University of Warwick, Gibbet Hill Road, Coventry CV4 7AL*

Accepted 2017 June 13. Received 2017 June 7; in original form 2016 December 28

## ABSTRACT

At the interface of H II regions and molecular gas, peculiar structures appear, some of them with pillar-like shapes. Understanding their origin is important for characterizing triggered star formation and the impact of massive stars on the interstellar medium. In order to study the molecular environment and influence of radiation on two pillar-like features related to the H II region G46.5–0.2, we performed molecular line observations with the Atacama Submillimeter Telescope Experiment and spectroscopic optical observations with the Isaac Newton Telescope. From the optical observations, we identified the star that is exciting the H II region as spectral type O4–6. The molecular data allowed us to study the structure of the pillars and an $HCO^+$ cloud lying between them. In this $HCO^+$ cloud, which has no well-defined $^{12}CO$ counterpart, we found direct evidence of star formation: two molecular outflows and two associated near-IR nebulosities. The outflow axis orientation is perpendicular to the direction of the radiation flow from the H II region. Several Class I sources are also embedded in this $HCO^+$ cloud, showing that it is usual that young stellar objects (YSOs) form large associations occupying a cavity bounded by pillars. On the other hand, it was confirmed that the radiation-driven implosion (RDI) process is not occurring in one of the pillar tips.

**Key words:** stars: formation – H II regions – ISM: jets and outflows – ISM: molecules – photodissociation region (PDR).

## 1 INTRODUCTION

H II regions can generate dense layers of gas and dust in their surroundings. Very often, in the interface between the photodissociation region (PDR) and the molecular gas, peculiar structures can appear, some of them with pillar-like shapes and cometary globules of dense gas. The pillars, also called 'elephant trunks', usually present a column-like structure with a head and a tail that connects physically with the molecular cloud. In our Galaxy, they typically have a size between 1 and 4 pc and a width between 0.1 and 0.7 pc (Gahm et al. 2006). Most of the mass in these pillars is concentrated in their heads, where, in some cases, signatures of star formation are found (Sugitani et al. 1989; Smith et al. 2010a; Smith, Bally & Walborn 2010b; Ohlendorf et al. 2013). The pillars were proposed to be transient features, being part of a continuous outwardly propagating wave of star formation driven by feedback from massive stars (Smith et al. 2010b). One of the main mechanisms of star formation in such regions is radiation-driven implosion (RDI), first proposed by Reipurth (1983). This process begins when the ionization front from the H II region moves over a molecular condensation such as the head of a pillar-like feature, creating a dense outer shell of ionized gas, the ionized boundary layer (IBL). If the IBL is overpressured with respect to the molecular gas within the head of the pillar, shocks are driven into it, compressing the molecular material until the internal pressure is balanced with the pressure of the IBL. At this stage, the collapse of the clump begins a process leading to the creation of a new generation of stars (Lefloch & Lazareff 1994; Bertoldi & McKee 1990). Recent theoretical and observational studies of pillars related to H II regions and possible star formation linked to them can be found in Hartigan et al. (2015) and Tremblin et al. (2012, 2013). These studies highlight the

★ E-mail: sparon@iafe.uba.ar

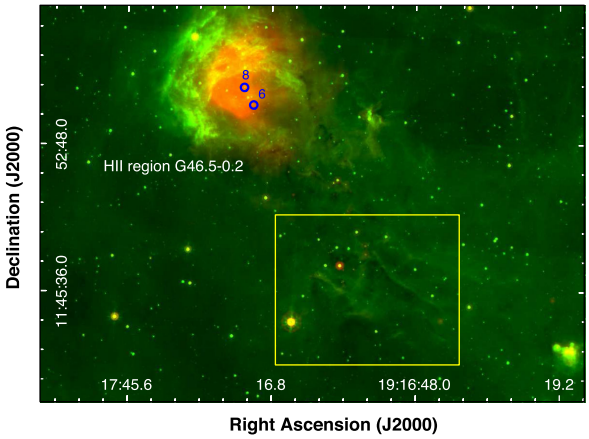


**Figure 1.** Two-colour composite image of a large area towards the field of the H II region G46 where the *Spitzer*–IRAC 8-μm emission is displayed in green and the *Spitzer*–MIPSGAL 24-μm emission in red. The blue circles are the stellar candidates to be the exciting sources of the H II region (sources 6 and 8 from Paper I). Towards the southwest of G46, the region studied in this work is delineated with a yellow rectangle. [A colour version of this figure is available in the online version.]

importance of understanding the origin of these structures in order to shed light on issues such as triggered star formation and the impact of massive stars on the initial mass function.

G46.5–0.2 (hereafter G46) is an H II region located at a distance of about 4 kpc and spanning an angular size of 8 arcmin (see Paron et al. 2015 and references therein). It lies on the border of the molecular cloud GRSMC G046.34–00.21 (Rathborne et al. 2009). In the south-west direction, about 10 arcmin away from G46 and associated with the molecular cloud, there are two pillar-like features that are bright at 8 μm and are oriented such that they point towards the open border of G46. Fig. 1 shows a two-colour composite image of the G46 field where the *Spitzer*–IRAC 8-μm emission is displayed in green and the *Spitzer*–MIPSGAL at 24 μm in red. The region of the pillar-like features is shown with a yellow rectangle. Based on the pillars' orientation and the similarity between the recombination line velocity of the H II region and the velocity of the molecular gas associated with the pillars, Paron et al. (2015, hereafter Paper I) proposed that G46 and the pillar-like features are located at the same distance. Thus it was concluded that the pillars were carved and sculpted by the ionizing flux from G46. Through a photometric analysis presented in Paper I, the authors look for candidates for the H II region exciting star(s). They find that sources 6 and 8 are the most likely ones to be O-type stars (blue circles in Fig. 1). In addition, two concentrations of young stellar object (YSO) candidates were found and considered to be embedded in the molecular cloud GRSMC G046.34–00.21. One of these YSO concentrations is closer to the G46 open border and consists of Class II type source candidates and the other is composed mostly of Class I type YSO candidates and is located just ahead of the pillar-like features, suggesting an age gradient in the YSO distribution. In an attempt to find a possible mechanism for star formation in the region, the authors performed a rough pressure balance study using publicly available $^{13}$CO $J = 1$–0 data (46 arcsec in angular resolution) towards the tips of the pillars. They found that the internal pressure of the neutral gas in the pillar-like feature heads is larger than the external pressure due to the ionized gas stalling at their tips, implying that RDI is not happening.

Taking into account that it is not common to find such large angular separation between H II regions and their related pillar structures and such a well-defined scenario without confusion from the usual clustering of H II regions as in G46, this is an interesting case to revisit using better data, in order to characterize the pillars physically and chemically and study the influence of radiation on them. This new study aims to determine whether the RDI process is ongoing or not and to find direct evidence of star formation activity associated with the pillars and their surroundings. Thus, using new molecular line observations obtained with the Atacama Submillimeter Telescope Experiment (ASTE), optical spectroscopic observations from the Intermediate Dispersion Spectrograph (IDS) at the Isaac Newton Telescope (INT) and public near- and mid-IR data, we performed a detailed study of the molecular environment towards the pillar-like features and the radiation flux arriving at them.

## 2 OBSERVATIONS AND DATA REDUCTION

### 2.1 Optical observations

In order to identify the source exciting G46 and obtain a more accurate estimate for the photon flux reaching the pillar tips, we performed spectroscopic optical observations of two stars, sources 6 and 8 from Paper I (blue circles in Fig. 1), which from photometric considerations were suspected to be O-type stars. These observations were performed on 2016 May 12 with the IDS at the Isaac Newton Telescope on La Palma, Spain. IDS observations were carried out using the EEV10 detector with the R632V grating (dispersion 0.9 Å pixel$^{-1}$) with a central wavelength at 4800 Å, providing a resolution of $R \sim 2500$. Exposure times were 2400 and 300 s for sources 8 and 6, respectively. The images were reduced and spectra extracted with the IRAF software[1] following the standard procedures for long-slit optical spectroscopic observations. The spectra, in digital counts, were normalized to infer the spectral types of the stars.

### 2.2 Molecular observations

The molecular observations were performed on 2015 August 25–27 with the 10-m ASTE telescope (Ezawa et al. 2004). The CATS345 GHz band receiver, a two-single band SIS receiver remotely tunable in the LO frequency range of 324–372 GHz, was used. The XF digital spectrometer was set to a bandwidth and spectral resolution of 128 MHz and 125 kHz, respectively. The spectral velocity resolution was 0.11 km s$^{-1}$ and the half-power beamwidth (HPBW) was 22 arcsec at 345 GHz. The system temperature varied in range $T_{sys} = 150$–250 K. The absolute intensity calibration was made with observations of W51D (19:23:39.85, +14:31:10.1, J2000) and the intensity variation was estimated to be less than 7 per cent. The main beam efficiency was $\eta_{mb} \sim 0.6$. The pointing accuracy was checked by observing RAql (19:06:22.254, +08:13:47.57, J2000) and was within 5 arcsec. The sky opacity varied from 0.04–0.06.

We observed a region of 5.8 × 5.1 arcsec$^2$ centred at 19:16:58.4, +11:45:41.6 (J2000) (blue box in Fig. 2), with a grid spacing of 22 arcsec in the $^{12}$CO $J = 3$–2 and HCO$^+$ $J = 4$–3 transitions,

[1] IRAF is distributed by the National Optical Astronomy Observatory, which is operated by the Association of Universities for Research in Astronomy (AURA) under a cooperative agreement with the National Science Foundation.

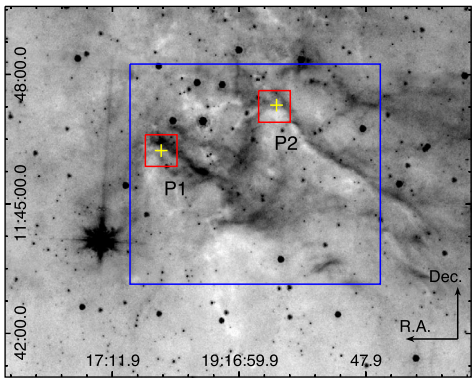


**Figure 2.** *Spitzer*-IRAC 8-μm emission of the pillar-like features with the regions observed with ASTE: the larger blue box was mapped in the $^{12}$CO $J = 3$–2 and HCO$^+$ $J = 4$–3 lines, the small red boxes in the HCN $J = 4$–3 line and the crosses are the positions of single pointings in the HNC $J = 4$–3, $^{13}$CO $J = 3$–2 and CS $J = 7$–6 lines.

with an integration time of 25 s per pointing. As shown in Fig. 2, the eastern pillar is called P1, while the western one is called P2. Additionally we observed two regions of 44 × 44 arcsec$^2$ with a grid spacing of 22 arcsec in the HCN $J = 4$–3 line (red boxes in Fig. 2). The centres of these regions are 19:16:56.6, +11:47:15.7 (J2000) (P1 head) and 19:17:07.3, +11:46:14.2 (J2000) (P2 head). The integration time was 500 s per pointing. We also observed the heads of the pillar-like features with single pointings in the HNC $J = 4$–3, $^{13}$CO $J = 3$–2 and CS $J = 7$–6 lines with an integration time of 500 s per pointing for HNC and 120 s per pointing for the other lines. The observed positions, marked with yellow crosses in Fig. 2, are 19:16:56.4, +11:47:17.5 (J2000) and 19:17:07.3, +11:46:15.0 (J2000). All observations were performed in position-switching mode.

The data were reduced with NEWSTAR[2] and the spectra processed using the XSPEC software package.[3] The spectra were Hanning-smoothed to improve the signal-to-noise ratio and in some cases a boxcar smoothing was also applied. Polynomials between first and third order were used for baseline fitting.

## 3 RESULTS

### 3.1 Identifying the stars causing g46 excitation

From the optical spectroscopic analysis of sources 6 and 8 (see Fig. 1), we determine that source 6 cannot be a contributor to the ionization of the region. Following Gray's Digital Spectral Classification Atlas,[4] its spectrum (Fig. 3, bottom panel) suggests that this source is a G-type star, which would be unable to generate an H II region. Source 8 suffers high extinction ($B - R \sim 3.6$), being relatively faint at blue wavelengths, hence the blue portion of the spectrum, which contains the He lines commonly used for O spectral classification, is very noisy. Nevertheless, in the range from 5400–5900 Å the lines of He II λ5411 and He I λ5876 are clearly visible (see Fig. 3, top panel). The ratio [He II]/[He I] from these two lines corresponds well to the spectral-type sequence, in which,

[2] Reduction software based on AIPS developed at NRAO, extended to treat single-dish data with a graphical user interface (GUI).
[3] XSPEC is a spectral line reduction package for astronomy, which has been developed by Per Bergman at Onsala Space Observatory.
[4] http://ned.ipac.caltech.edu/level5/Gray/frames.html

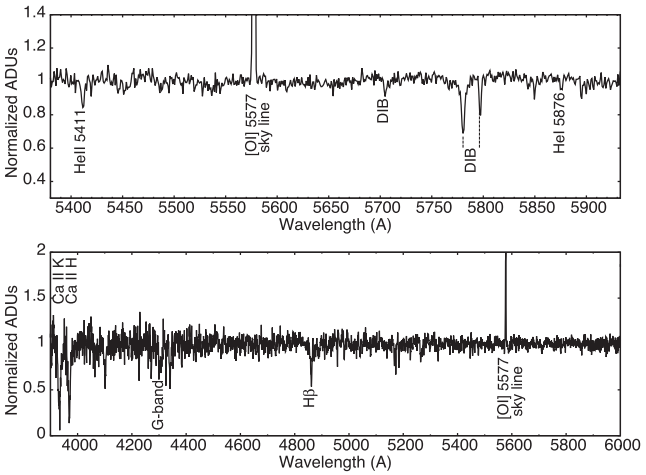


**Figure 3.** Top: portion of the optical spectrum of source 8 where the absorption lines of He II λ5411 and He I λ5876 are present. Some of the unlabelled absorption features are from diffuse interstellar bands (e.g. Lan, Ménard & Zhu 2015). Bottom: optical spectrum of source 6, which, following Gray's Digital Spectral Classification Atlas, corresponds to a G-type star.

according to Walborn (1980), He I λ5876 is present from type O4 to later types and a ratio ∼1 corresponds to type O7. Therefore, according to the observed ratio [He II λ5411]/[He I λ5876] for source 8 and comparing with ratios of [He II λ4541]/[He I λ4471] and [He II λ4541]/[He I λ4387] in Walborn & Fitzpatrick (1990), we can infer that source 8 is a O4–6 star.

### 3.2 Molecular environment related to the pillars

As studied in Paper I and mentioned here in Section 1, the velocities of the molecular gas concentrations related to the pillars are similar to the recombination line velocity of the H II region G46, thus throughout this work it is assumed that all of these structures are located at the same distance.

We analysed the $^{12}$CO $J = 3$–2 data cube along the whole velocity axis, in order to find molecular structures associated with the pillar-like features delineated by the IR emission at 8 μm. In Fig. 4, the $^{12}$CO integrated emission is presented in channel maps in steps of 1.1 km s$^{-1}$ along the velocity interval from 41–60 km s$^{-1}$. The positions of the pillar heads are indicated with crosses in each panel. Abundant molecular gas towards the north of the surveyed region and not related to the pillars can be distinguished in the range 43–53 km s$^{-1}$. Between 43.5 and 48.9 km s$^{-1}$, there is an interesting structure with a bilobed shape towards the north-east lying between both pillars, which will be studied in Section 3.3. It can be appreciated that in the velocity interval 53.3–56.5 km s$^{-1}$ there are some molecular structures that are likely associated with the pillar-like features, while at other velocities they appear as clumpy molecular structures without any morphological correspondence with the pillars.

The molecular structures associated with the pillars extend along narrow velocity intervals. This is shown in Fig. 5, where the molecular gas emission is superimposed on the 8-μm emission. The most remarkable morphological association between the molecular gas and the 8-μm emission is between 55.3 and 56.5 km s$^{-1}$ in pillar P2 (right panel in the figure). Then, between 53.0 and 55.3 km s$^{-1}$ (middle panel), there is a weak feature related to P2 and another one associated with P1 with a peak towards its base. A clump associated with the P1 tip appears between 52.5 and 53.0 km s$^{-1}$ (left panel),

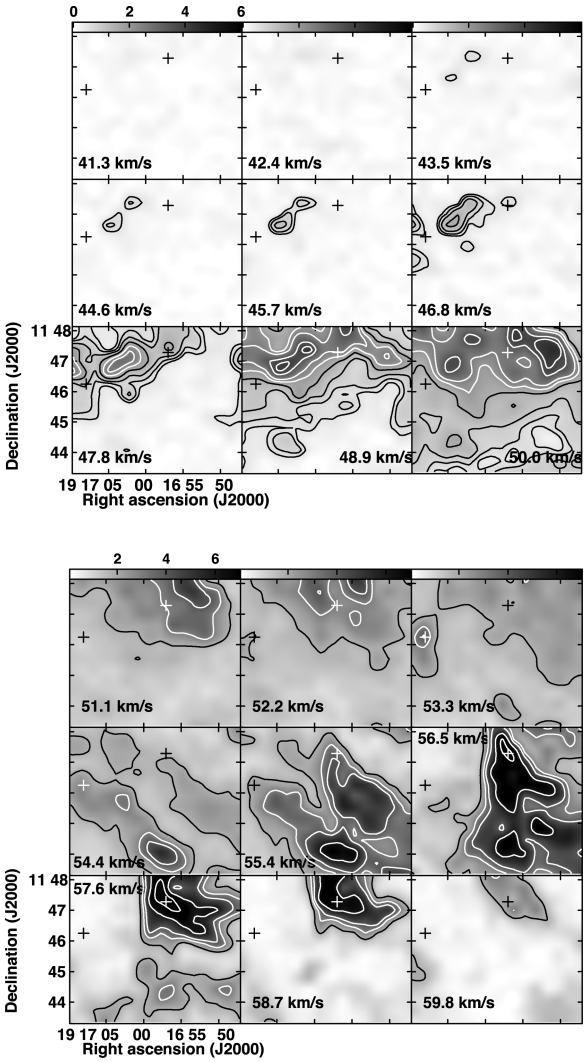


**Figure 4.** $^{12}$CO $J = 3$–2 velocity integrated channel maps each 1.1 km s$^{-1}$ of the surveyed region, are shown in two images. From 41.3–50.0 km s$^{-1}$ with contours levels of 0.5, 0.7, 1.0, 1.5, 2.0, 2.5, 3.5 and 4.0 K km s$^{-1}$ (upper image) and from 51.1–59.8 km s$^{-1}$ with 1.8, 3.0, 4.0, 6.0 and 8.0 K km s$^{-1}$ (bottom image). The intensity range is shown at top of each image and is in K km s$^{-1}$. The crosses are the positions of the pillar heads.

showing that the molecular gas associated with this pillar is more clumpy than the gas associated with P2.

Fig. 6 shows the $^{12}$CO and $^{13}$CO spectra obtained at the location of the yellow crosses shown in Fig. 2, i.e. the heads of the pillar-like features. The CS $J = 7$–6 emission was not detected at these positions. Table 1 lists the line parameters obtained from Gaussian fits to these spectra (superimposed in red in the figure). The $^{12}$CO spectrum from the head of P1 was fitted with three Gaussians. Two main components within the velocity range 45–55 km s$^{-1}$ can be seen, with a smaller component centred at ∼60 km s$^{-1}$. The $^{13}$CO spectrum is less complex and could be fitted with two Gaussians, the counterparts of the $^{12}$CO main components. In the case of the P2 head, both CO isotopes were fitted with two Gaussians, showing the presence of two molecular components towards this region.

To derive the molecular mass contained in the heads of the pillar-like features, local thermodynamic equilibrium (LTE) was assumed. Following the standard LTE procedures, we obtain a $^{12}$CO column density, $N(^{12}\mathrm{CO})$, for each pillar head. For the details of the formulae see e.g. Paron et al. (2012). From the ratio of the $T_{\rm mb}(^{12}\mathrm{CO})$ to $T_{\rm mb}(^{13}\mathrm{CO})$ peaks, the $^{12}$CO and $^{13}$CO optical depths ($\tau_{12}, \tau_{13}$) can be derived. As shown in Fig. 6 and Table 1, the $^{12}$CO and $^{13}$CO spectra have more than one component and thus at least a couple of $\tau_{12}$ and $\tau_{13}$ could be obtained for each pillar head. By inspecting the central velocities and $\Delta v$ of each component (see Table 1), we selected the $T_{\rm mb}(^{12}\mathrm{CO})$ and $T_{\rm mb}(^{13}\mathrm{CO})$ peaks that are within the velocity intervals into which each pillar extends (see Fig. 4), thus we used the components at ∼55 and ∼58 km s$^{-1}$ for P1 and P2, respectively. Assuming a canonical [$^{12}$CO]/[$^{13}$CO] isotope abundance ratio of 50, we estimate the optical depths $\tau_{12} \sim 89$ and $\tau_{13} \sim 1.7$ for the P1 head and $\tau_{12} \sim 25$ and $\tau_{13} \sim 0.5$ for the P2 head. Due to the high optical depth of the $^{12}$CO emission, it is not possible to obtain reliable mass values from the $^{12}$CO column density. Thus, using the derived $\tau_{13}$ values, we calculate the $^{13}$CO column densities from each single pointing at P1 and P2. The excitation temperature ($T_{\rm ex} \sim 10$ K used in both cases) was obtained from the $^{12}$CO spectra at the tips of each pillar. Assuming that the $^{13}$CO emission is uniformly distributed in the pillar heads, i.e. that the column density value is the same at all beam positions within a circle delimited by the curvature of the tip of the pillars, we estimate a total $^{13}$CO column density for each pillar head. Finally, the $H_2$ column densities were derived from $N(\mathrm{H_2}) = N(^{13}\mathrm{CO})/X_{^{13}\mathrm{CO}}$, where $X_{^{13}\mathrm{CO}} = 2 \times 10^{-6}$ (e.g. Yamaguchi et al. 1999), and the mass is derived from

$$\mathrm{M} = \mu m_{\rm H} D^2 \Omega N(\mathrm{H_2}), \quad (1)$$

where Ω is the solid angle subtended by the beam size, $D$ is a distance of 4 kpc, $m_{\rm H}$ is the hydrogen mass and $\mu$ is the mean

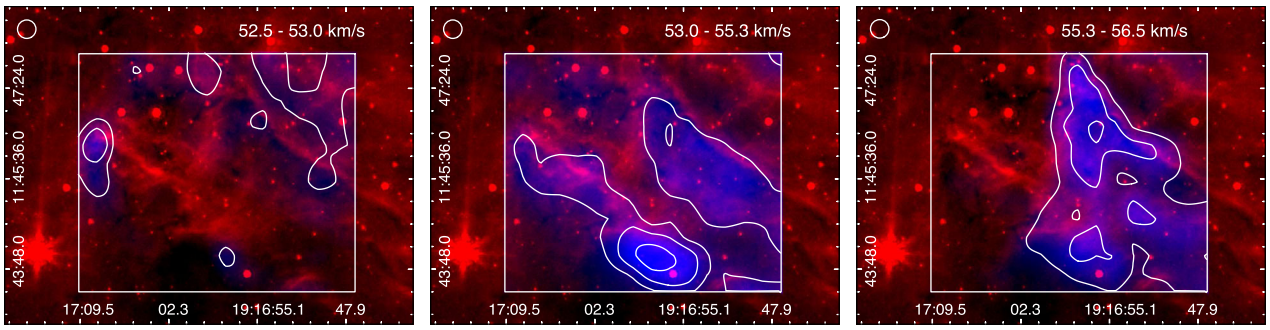


**Figure 5.** $^{12}$CO $J = 3$–2 velocity integrated maps (blue with white contours) displayed over the IRAC–*Spitzer* 8-μm emission (red). The integration velocity interval is shown at the top of each panel and the beam of the molecular observations is included to the top left corner. The contour levels are 0.7 and 0.9 K km s$^{-1}$ (left), 3.6, 5.0 and 7.0 K km s$^{-1}$ (middle) and 3.0 and 4.9 K km s$^{-1}$ (right). [A colour version of this figure is available in the online version.]

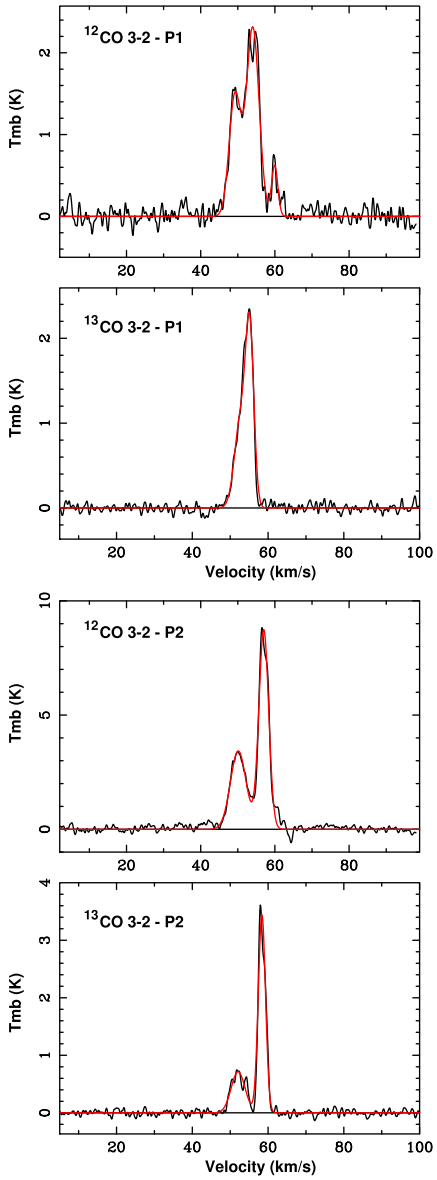


**Figure 6.** $^{12}$CO and $^{13}$CO spectra observed in the region of the heads of the pillar-like features (yellow crosses in Fig. 2). The Gaussian fitting to each spectrum is shown in red. The rms noise is about 100 and 50 mK for the $^{12}$CO and $^{13}$CO lines, respectively. [A colour version of this figure is available in the online version.]

**Table 1.** Line parameters for the CO isotopes.

| Line | $T_{mb}$ (K) | $v_{LSR}$ (km s$^{-1}$) | $\Delta v$ (km s$^{-1}$) |
|---|---|---|---|
| $^{12}$CO (3–2) – P1 | 1.48 | 49.23 | 3.70 |
| | 2.30 | 54.03 | 5.00 |
| | 0.62 | 59.94 | 1.97 |
| $^{13}$CO (3–2) – P1 | 1.06 | 52.82 | 3.83 |
| | 1.91 | 55.20 | 2.53 |
| $^{12}$CO (3–2) – P2 | 3.43 | 50.13 | 4.97 |
| | 8.73 | 57.00 | 3.10 |
| $^{13}$CO (3–2) – P2 | 0.71 | 52.10 | 4.30 |
| | 3.44 | 58.36 | 2.24 |

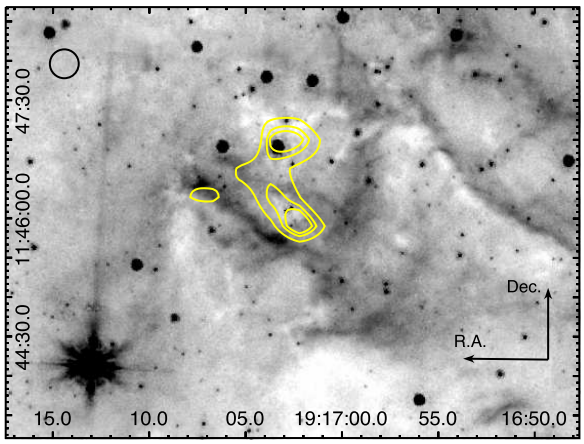


**Figure 7.** The HCO$^+$ $J$ = 4–3 emission integrated between 48 and 60 km s$^{-1}$ is displayed in contours over the *Spitzer*–IRAC 8-μm emission. The contour levels are 0.5, 0.6 and 0.7 K km s$^{-1}$. The beam of the molecular observation is included in the top left corner. [A colour version of this figure is available in the online version.]

molecular weight, assumed to be 2.8 by taking into account the relative helium abundance of 25 per cent. The masses obtained for the heads of P1 and P2 are about 60 $M_\odot$ and 30 $M_\odot$, respectively.

Analysing the HCO$^+$ $J$ = 4–3 cube, we found emission in a region between the pillar-like features (see Fig. 7). The HCO$^+$ structure is composed of two clumps (hereafter HCO$^+$ northern and southern clumps). The centre of the northern one coincides in projection with the peak of the 1.1-mm emission source BGPS G046.319–00.233 (Rosolowsky et al. 2010) and with the $^{12}$CO bilobed structure described above. Besides this positional coincidence, it is worth noting that at the HCO$^+$ structure position, i.e. the region between both pillars, there is not a well-defined $^{12}$CO structure (see Fig. 4). In addition, some weak HCO$^+$ emission appears towards the head of P1, in coincidence with the source BGPS G046.319–00.255. At this position we also detected HNC $J$ = 4–3, which is shown in Fig. 8, together with the HCO$^+$ spectra towards the peak of the mentioned BGPS sources and the southern HCO$^+$ clump. The line parameters obtained from Gaussian fits to these spectra are presented in Table 2. Towards the head of P2, which also coincides with a millimetre continuum source (BGPS G046.314–00.213), HCO$^+$ $J$ = 4–3 was not detected. Finally, HCN $J$ = 4–3 emission was not detected in either of the pillar-like features.

With the parameters obtained from our data and those for the HCO$^+$ $J$ = 3–2 from Shirley et al. (2013) also included in Table 2, we performed a non-LTE study of the P1 head and the northern HCO$^+$ clump using the RADEX code (van der Tak et al. 2007). In order to compare both sets of data, our HCO$^+$ $J$ = 4–3 spectra were convolved with a beam of 30 arcsec from the Shirley et al. HCO$^+$ $J$ = 3–2 observations. The RADEX calculations were made for different kinetic temperatures in the range between 20 and 100 K. The results are presented in Table 3. In the case of the P1 head, RADEX does not converge for $T_k$ = 100 K.

Additionally, we estimate the dust temperature, $T_d$, and the $H_2$ column density for the P1 head and the HCO$^+$ northern clump from the *Herschel* public data at 160, 250, 350, and 500 μm (OBsId 1342207054 and 1342207055) and the ATLASGAL data at 870 μm (from Urquhart et al. 2014). Assuming dust emission in the optically thin regime, the surface brightness, $I_\nu$, can be expressed as a greybody function for a single temperature:

$$I_\nu = \kappa_\nu (\nu/\nu_0)^\beta B_\nu(T_{dust}) \mu m_H N(H_2), \quad (2)$$

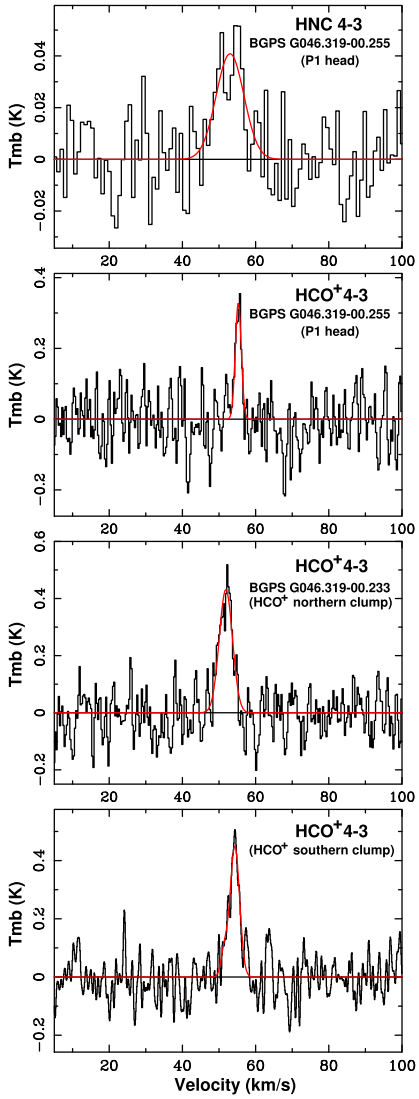


**Figure 8.** First and second panels: HNC and $HCO^+$ $J = 4$–3 spectra obtained in the region of the P1 head, at the position of BGPS G046.319–00.255. Third and fourth panels: $HCO^+$ $J = 4$–3 spectra at the peak position of BGPS G046.319–00.233 at the northern $HCO^+$ clump and at the southern $HCO^+$ clump, respectively (see Fig. 7). A Gaussian fit of each spectrum is shown in red. The rms noise for these spectra is 13 and 45 mK for the HNC and $HCO^+$ lines, respectively.

where $B_\nu(T_{\rm dust})$ is the blackbody function for a dust temperature $T_{\rm dust}$, $\mu$ the conversion factor from $H_2$ to total gas mass, assumed to be 2.8 by considering an He abundance of 25 per cent, $m_{\rm H}$ the atomic hydrogen mass and $\kappa_\nu(\nu/\nu_0)^\beta$ the dust opacity per unit mass, where $\nu_0$ is assumed to be 0.1 cm$^2$ g$^{-1}$ at 1 THz (Beckwith et al. 1990) under a gas-to-dust ratio of 100 and $\beta = 2$ (Anderson et al. 2012). Then, we performed an spectral energy distribution (SED) fitting with $T_{\rm dust}$ and $N(H_2)$ as free parameters, where the surface brightness was obtained from the level 2.5 *Herschel* data and from the catalogued ATLASGAL sources. All emission was convolved to the same resolution 44 arcsec and rebinned to the same pixel size 14 arcsec. We determined that $T_{\rm d}$ and $N(H_2)$ are about 18 K and $1.8 \times 10^{22}$ cm$^{-2}$ and 20 K and $0.8 \times 10^{22}$ cm$^{-2}$ for the $HCO^+$ northern clump and the P1 head, respectively. The errors involved in the temperatures and column densities are about 10 and 40 per cent, respectively. From these results, if we assume

**Table 2.** Line parameters for the $HCO^+$ and HNC lines.

| Line | $T_{\rm mb}$ (K) | $v_{\rm LSR}$ (km s$^{-1}$) | $\Delta v$ (km s$^{-1}$) | $\int T_{\rm mb}\,{\rm d}v$ (K km s$^{-1}$) |
|---|---|---|---|---|
| BGPS G046.319–00.233 ($HCO^+$ northern clump) | | | | |
| $HCO^+$ (4–3) | 0.43 | 51.87 | 4.25 | 1.87 |
| $HCO^+$ (3–2)* | 0.53 | 52.40 | 3.80 | 2.27 |
| ($HCO^+$ southern clump) | | | | |
| $HCO^+$ (4–3) | 0.45 | 54.32 | 3.05 | 1.68 |
| BGPS G046.319–00.255 (P1 head) | | | | |
| $HCO^+$ (4–3) | 0.33 | 55.26 | 1.90 | 0.68 |
| $HCO^+$ (3–2)* | 0.35 | 54.70 | 3.20 | 1.03 |
| HNC (4–3) | 0.04 | 53.02 | 8.90 | 0.37 |

*From Shirley et al. (2013).

**Table 3.** RADEX results.

| $T_{\rm k}$ (K) | $N$ (cm$^{-2}$) | $n$ (cm$^{-3}$) |
|---|---|---|
| BGPS G046.319–00.233 ($HCO^+$ northern clump) | | |
| 20 | $9.7 \times 10^{11}$ | $4.9 \times 10^6$ |
| 30 | $9.3 \times 10^{11}$ | $1.7 \times 10^6$ |
| 50 | $9.6 \times 10^{11}$ | $7.3 \times 10^5$ |
| 100 | $1.1 \times 10^{12}$ | $3.2 \times 10^5$ |
| BGPS G046.319–00.255 (P1 head) | | |
| 20 | $7.1 \times 10^{11}$ | $1.4 \times 10^6$ |
| 30 | $8.5 \times 10^{11}$ | $5.3 \times 10^5$ |
| 50 | $1.7 \times 10^{12}$ | $1.2 \times 10^5$ |
| 100 | – | – |

that the dust and gas are coupled and thus $T_{\rm d} = T_{\rm k}$, we can favour the RADEX results for $T_{\rm k} = 20$ K for both molecular concentrations. In this way we estimate the $HCO^+$ abundances $X_{HCO^+} \sim 5.4 \times 10^{-11}$ and $\sim 8.8 \times 10^{-11}$ for the $HCO^+$ northern clump and P1 head, respectively.

Additionally, from the same SED fitting procedure we obtained $T_{\rm dust}$ and $N(H_2)$ for the P2 head (source BGPS G046.314–00.213) of about 18 K and $1 \times 10^{22}$ cm$^{-2}$. Using the $N(H_2)$ obtained in P1 and P2 from the SED fitting in equation (1), we estimate the masses in an independent way as done above with the $^{13}$CO emission, obtaining about 80 $M_\odot$ for both pillar heads.

### 3.3 Direct evidence of star formation in the region

Given that in Paper I the existence of several YSO candidates in the region between the pillars was shown, we inspected the *Ks*-band emission obtained from the UKIDSS Survey (Lawrence et al. 2007), looking for signatures of extended emission likely to be related to outflow activity. We found an interesting structure composed of two nebulosities extending from south-east to north-west lying at the $HCO^+$ northern clump related to the BGPS G046.319–00.233 source (see Fig. 9). The figure also demonstrates that both nebulosities are separated by a region of low *Ks* emission. Interestingly, this near-IR structure lies at the same position of the north-eastern bilobed molecular feature that appears between 43.5 and 48.9 km s$^{-1}$ shown in Fig. 4. By integrating the $^{12}$CO emission along the velocity range 42–50 km s$^{-1}$, two conspicuous molecular lobes appear (blue contours in Fig. 9) that extend, as the near-IR

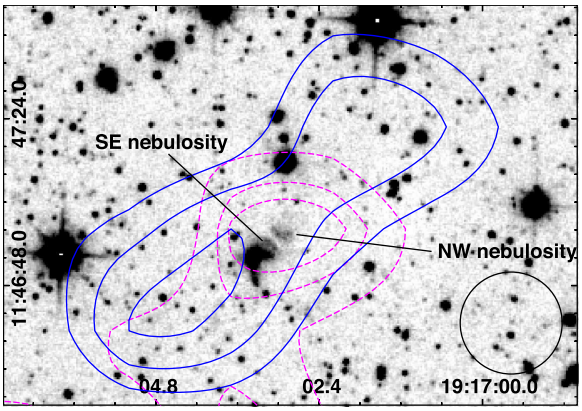


**Figure 9.** *Ks*-band emission obtained from the UKIDSS Survey with blue contours of the $^{12}$CO $J = 3$–2 emission integrated between 42 and 50 km s$^{-1}$ with levels of 6.0, 7.0 and 8.5 K km s$^{-1}$. The dashed magenta contours are the same HCO$^+$ contours as presented in Fig. 7. The beam of the molecular observation is included in the bottom right corner.

features, from south-east to north-west. The near-IR features mentioned above are located, in projection, almost at the centre of these lobes, which strongly suggests that we are observing molecular outflows generated by the same source that produced the near-IR features. The lengths of the outflows are 50 and 44 arcsec for the north-western and south-eastern lobes, respectively, which at a distance of 4 kpc implies about 0.9 and 0.8 pc, respectively.

To estimate the outflow mass, following Bertsch et al. (1993), we calculated the $H_2$ column density from

$$N(\mathrm{H_2}) = 2.0 \times 10^{20} \frac{W(^{12}\mathrm{CO})}{[\mathrm{K\ km\ s^{-1}}]}\ (\mathrm{cm^{-2}}), \quad (3)$$

where $W(^{12}\mathrm{CO})$ is the $^{12}$CO $J = 3$–2 integrated intensity. The mass was derived from equation (1), obtaining 10.5 and 9.0 $M_\odot$ for the south-eastern and north-western lobes respectively.

## 4 DISCUSSION

From the new molecular data presented in this work, we confirm that the gas related to the pillar-like features embedded in the large molecular cloud GRSMC G046.34–00.21 and associated with the H II region G46 extends along narrow velocity intervals. These pillars contain embedded cold submm cores, as were found towards similar structures in the Eagle Nebula (White et al. 1999). The derived masses for P1 and P2 heads from the new molecular observations are about 60 and 30 $M_\odot$, respectively. These values are in quite good agreement with the mass obtained from the dust emission (about 80 $M_\odot$ in both pillar heads). It is worth noting that these values are one order of magnitude lower than those obtained in Paper I using the $^{13}$CO $J = 1$–0 line. Given that this discrepancy is large and cannot be explained simply through the use of different lines, the values from Paper I were revised. After a careful inspection of the mass estimate procedure performed in Paper I, we noticed that a larger area than the actual extension of the pillar heads was wrongly used, yielding overestimated values. The actual mass values derived from the $^{13}$CO $J = 1$–0 line are between 60 and 80 $M_\odot$ for both pillar heads, in complete agreement with the values obtained here. It is important to remark that the volumetric density values in Paper I do not change significantly and hence the RDI analysis and its conclusion do not change.

We conclude that the mass of the pillar heads ranges from ∼30 to ∼80 $M_\odot$, which is in agreement with the masses of pillar heads found in several regions (Gahm et al. 2006; White et al. 1999) and with values obtained from 3D dynamical models used to study the formation of these kinds of structures (Mackey & Lim 2010).

In this work, we have mainly analysed three molecular structures: the pillar-like features P1 and P2 and a cloud observed in the HCO$^+$ $J = 4$–3 line lying between both pillars and composed of two clumps. Even though these features are embedded in the same large molecular cloud, we found different physical conditions between them. We suggest that this could be due to the fact that these features may be exposed in different ways to UV radiation. It is possible that P2 is more exposed to the radiation flow from G46 than P1. The non-detection of HCO$^+$ towards P2 and the HCO$^+$ abundances obtained in P1 and the HCO$^+$ northern clump may be explained through different ionization rates within the region. As is stated in Goicoechea et al. (2009), HCO$^+$ is mainly destroyed via dissociative recombination and thus its abundance is inversely proportional to the electron abundance. The structures belonging to the large and clumpy molecular cloud that are more exposed to radiation from the H II region are expected to have a higher electron abundance than the less exposed ones. We remark that this is quite a simple conclusion based only on the HCO$^+$ analysis and, as Goicoechea et al. (2009) pointed out, it is necessary also to consider the abundances of metals, PAHs, other ions and cosmic rays. In the case of the HCO$^+$ northern clump this situation is more complex, because, as presented and discussed in Sections 3.3 and 4.2, this clump presents outflow activity, which according to Rawlings et al. (2004) may increase the HCO$^+$ abundance. Nevertheless, our result gives support to different ionization rates along the region.

From the optical spectroscopic results of the star named source 8 (an O4–6 type star), together with the previous photometric analysis (see Paper I) and considering its location, exactly at the centre of the G46 H II region, we can conclude that this source is indeed responsible for the ionization of the region. This more accurate determination of the spectral type of the ionizing star allows us to derive a better estimate of the amount of UV photons arriving at the pillars. Given that P2 could be the structure more exposed to radiation from the H II region, the analysis was performed only for this structure. Following the same procedure as described in Paper I, we estimate an upper limit for the predicted photon flux impinging on the P2 head of $\phi_{\mathrm{pred}} \sim 3 \times 10^8$ cm$^{-2}$s$^{-1}$. Thus, according to Bisbas et al. (2011), who suggested that triggered star formation through RDI occurs only when $10^9$ cm$^{-2}$ s$^{-1}$ $\leq \phi \leq 3 \times 10^{11}$ cm$^{-2}$ s$^{-1}$, we can conclude that in the head of P2 it is unlikely that triggered star formation is ongoing.

### 4.1 HCN and HNC in the pillars

The HCN $J = 4$–3 line was not detected in any pillar and the HNC $J = 4$–3 line was detected only at the P1 tip. Taking into account that usually both isomers are detected in the same region and it is expected that the HNC/HCN ratio is of the order of unity in cold regions (Herbst 1978; Schilke et al. 1992), it is intriguing to consider why at the P1 tip, a region that coincides with a catalogued dark cloud, HNC is detected and not HCN. It could be that the HNC has higher abundance than the HCN, with the HCN abundance being low enough to be below the detection limit for these observations. This is indeed possible because, according to Hirota et al. (1998), the recombination reaction HCNH$^+$ + e$^-$ → HNC + H, HCN + H, one of the main possible chemical paths for the formation of these isomers, leads to a higher abundance of HNC than of HCN.

On the other hand, Chenel et al. (2016) point out that in interstellar regions exposed to an intense UV radiation field HCN should be more abundant than HNC. The destruction of both isomers in such regions is dominated by photodissociation rather than chemical reactions with radicals or ions and the authors found that HNC is destroyed faster than HCN. In the case of the P1 head, it is likely that this structure is not strongly irradiated by UV photons and hence the UV destruction mechanism is not ongoing. At the P2 head, which may be more exposed to radiation, it could be possible that the HCN and HNC have been totally destroyed by UV radiation. This is in agreement with the results from the $HCO^+$ analysis discussed in the previous section.

### 4.2 Confirming star formation

We find direct evidence of star formation at the $HCO^+$ northern clump in both near-IR and molecular line emission. The near-IR emission shows the presence of two nebulosities separated by a region of low emission. Taking into account that the molecular outflows discovered extend along the same direction as the near-IR nebulosities, we suggest that the IR emission arises from cavities cleared in the circumstellar material. This kind of cavity can be generated by the action of winds from the YSO (Shu et al. 1995; Reipurth & Bally 2001) or by precessing jets that clear the circumstellar material (e.g. Kraus et al. 2006). The orientation of the nebulosities and analysis of the molecular lobes strongly suggests that the outflows extend mainly in the plane of the sky. This may explain why a central point source is not seen in near-IR emission, it being probable that we are observing the YSO system in an edge-on orientation and the central source is likely hidden behind the disc (e.g. Perrin et al. 2006). In this scenario, the central source and the disc must lie in the region of low near-IR emission between the two nebulosities. This YSO system and most of the Class I YSO candidates found in Paper I are embedded in the mapped $HCO^+$ cloud lying between both pillars, which, based on what was observed by Smith et al. (2010a) in the Carina Nebula, seems to be common. As the authors concluded, the YSOs tend to form large associations occupying a cavity that is bounded by pillars. It is important to note that the observed $HCO^+$ cloud does not have a well-defined counterpart in the $^{12}CO$ emission, suggesting that the external layers of the molecular gas traced by the $^{12}CO$ emission were disrupted by massive star feedback.

The mass and size of the molecular outflows discovered are similar to those found for several sources catalogued as massive molecular outflows (Beuther et al. 2002), suggesting that we are indeed observing a massive YSO. It is worth noting that its outflow axis orientation is perpendicular to the direction of the H II region open border and hence to the direction of the radiation flow. This orientation was also found in several YSOs in the Carina Nebula (Smith et al. 2010a). Using 3D simulations, Lora, Raga & Esquivel (2009) proposed interaction between an advancing ionization front and a neutral cloud, wherein compressed clumps of gas that form at the unstable interface tend to collapse and have angular momentum vectors perpendicular to the direction of the radiation flow. The YSO system described here could be considered as new observational evidence of this phenomenon, suggesting the need for further theoretical studies in which the large distance (about 10 pc) between the YSO and the radiation source should be taken into account.

## 5 SUMMARY AND CONCLUDING REMARKS

Using the ASTE telescope and public IR data, we investigated in detail the molecular environment related to two pillar-like features likely generated by the H II region G46.5–0.2 (G46). Additionally, using the INT telescope we found the star that is exciting this H II region. The main results of this study are summarized as follows.

(1) From the $^{12}CO$ $J = 3$–2 emission, we found that the molecular structure of the pillar-like features extends along narrow velocity intervals. It was observed that P2 has the expected morphology of the pillars, while the molecular emission at P1 is more clumpy and the main mass concentration is not in its head. P1 may be in an earlier evolutionary stage in the formation of this kind of pillar.

(2) The $HCO^+$ $J = 4$–3 emission was found to be concentrated in a cloud lying between both pillars and composed of two clumps. This cloud has no well-defined $^{12}CO$ counterpart. Faint $HCO^+$ emission was detected towards the head of P1, where HNC $J = 4$–3 emission was also detected. At the P2 tip, emission from these species was not detected. From a $HCO^+$ abundance analysis, it is suggested that P2 could be more exposed to the radiation from G46 than P1.

(3) From optical spectroscopic observation, it was determined that the so-called source 8 (from Paper I) is an O4–6 star. Thus, from its position and spectral type we conclude that this is the source responsible for ionizing the region.

(4) From the spectral type determination of the ionizing source, we obtained a more accurate value for the amount of UV flux arriving at P2. We conclude that it is unlikely that the RDI process is ongoing in the P2 head.

(5) We found direct evidence of star formation towards the cloud mapped in the $HCO^+$ emission. From the $^{12}CO$ $J = 3$–2 line, we detected two massive molecular outflows extended mainly along the plane of the sky, coinciding with two nebulosities separated by a region of low emission seen at near-IR emission. We propose that we are observing a YSO system in an edge-on position.

The confirmed star formation activity in the region analysed is occurring in a molecular clump that it is bounded by the pillar-like features, which seem to be commonly found in such regions, confirming that the pillars are transient structures that are part of a continuous outwardly propagating wave of star formation driven by the feedback from massive stars, as proposed by Smith et al. (2010b). The mapped $HCO^+$ cloud, in which the discovered outflow source and most of the Class I sources shown in Paper I are embedded, has no well-defined counterpart in the $^{12}CO$ emission. This suggests that the external layers of the molecular cloud were disrupted by radiation from G46, which is in agreement with a scenario of star formation driven by the radiation from massive stars. Additionally, we found that the outflow axis orientation of the discovered YSO is perpendicular to the direction of the radiation flow, in agreement with the results of simulations performed by Lora et al. (2009). Taking into account the large distance (about 10 pc) between the massive star and the YSO, this could be important observational evidence to motivate the study of this phenomenon in such radiation sources/YSO configurations.

These new results strengthen the suggestion presented in Paper I of a star formation gradient generated by the action of the H II region G46, in which the formation processes have stopped at the pillar tips.

## ACKNOWLEDGEMENTS

We thank the anonymous referee for very helpful comments and suggestions. The ASTE project is led by Nobeyama Radio Observatory (NRO), a branch of National Astronomical Observatory of Japan (NAOJ), in collaboration with University of Chile and Japanese institutes including University of Tokyo, Nagoya

University, Osaka Prefecture University, Ibaraki University, Hokkaido University and the Joetsu University of Education. The INT is operated on the island of La Palma by the Isaac Newton Group in the Spanish Observatorio del Roque de los Muchachos of the Instituto de Astrofísica de Canarias. SP, MO and AP are members of the *Carrera del investigador científico* of CONICET, Argentina. MCP is a doctoral fellow of CONICET, Argentina. This work was partially supported by grants awarded by CONICET, ANPCYT and UBA (UBACyT) from Argentina. AP acknowledges support from the Varsavsky Foundation. MR acknowledges support from FONDECYT(CHILE) grant No. 1140839. SP and AP are grateful to Dr Takeshi Okuda for the support received during the ASTE observations.

## REFERENCES

Anderson L. D. et al., 2012, A&A, 542, A10
Beckwith S. V. W., Sargent A. I., Chini R. S., Guesten R., 1990, AJ, 99, 924
Bertoldi F., McKee C. F., 1990, ApJ, 354, 529
Bertsch D. L., Dame T. M., Fichtel C. E., Hunter S. D., Sreekumar P., Stacy J. G., Thaddeus P., 1993, ApJ, 416, 587
Beuther H., Schilke P., Sridharan T. K., Menten K. M., Walmsley C. M., Wyrowski F., 2002, A&A, 383, 892
Bisbas T. G., Wünsch R., Whitworth A. P., Hubber D. A., Walch S., 2011, ApJ, 736, 142
Chenel A., Roncero O., Aguado A., Agúndez M., Cernicharo J., 2016, J. Chem. Phys., 144, 144306
Ezawa H., Kawabe R., Kohno K., Yamamoto S., 2004, in Oschmann J. M., Jr, ed., Proc. SPIE Vol. 5489. Society of Photo-Optical Instrumentation Engineers. SPIE, Bellingham, p 763.
Gahm G. F., Carlqvist P., Johansson L. E. B., Nikolić S., 2006, A&A, 454, 201
Goicoechea J. R., Pety J., Gerin M., Hily-Blant P., Le Bourlot J., 2009, A&A, 498, 771
Hartigan P., Reiter M., Smith N., Bally J., 2015, AJ, 149, 101
Herbst E., 1978, ApJ, 222, 508
Hirota T., Yamamoto S., Mikami H., Ohishi M., 1998, ApJ, 503, 717
Kraus S. et al., 2006, A&A, 455, 521
Lan T.-W., Ménard B., Zhu G., 2015, MNRAS, 452, 3629
Lawrence A. et al., 2007, MNRAS, 379, 1559
Lefloch B., Lazareff B., 1994, A&A, 289, 559
Lora V., Raga A. C., Esquivel A., 2009, A&A, 503, 477
Mackey J., Lim A. J., 2010, MNRAS, 403, 714
Ohlendorf H., Preibisch T., Gaczkowski B., Ratzka T., Ngoumou J., Roccatagliata V., Grellmann R., 2013, A&A, 552, A14
Paron S., Ortega M. E., Petriella A., Rubio M., Dubner G., Giacani E., 2012, MNRAS, 419, 2206
Paron S. et al., 2015, AJ, 149, 193
Perrin M. D., Duchêne G., Kalas P., Graham J. R., 2006, ApJ, 645, 1272
Rathborne J. M., Johnson A. M., Jackson J. M., Shah R. Y., Simon R., 2009, ApJS, 182, 131
Rawlings J. M. C., Redman M. P., Keto E., Williams D. A., 2004, MNRAS, 351, 1054
Reipurth B., 1983, A&A, 117, 183
Reipurth B., Bally J., 2001, ARA&A, 39, 403
Rosolowsky E. et al., 2010, ApJS, 188, 123
Schilke P., Walmsley C. M., Pineau Des Forets G., Roueff E., Flower D. R., Guilloteau S., 1992, A&A, 256, 595
Shirley Y. L. et al., 2013, ApJS, 209, 2
Shu F. H., Najita J., Ostriker E. C., Shang H., 1995, ApJ, 455, L155
Smith N. et al., 2010, MNRAS, 406, 952
Smith N., Bally J., Walborn N. R., 2010, MNRAS, 405, 1153
Sugitani K., Fukui Y., Mizuni A., Ohashi N., 1989, ApJ, 342, L87
Tremblin P., Audit E., Minier V., Schmidt W., Schneider N., 2012, A&A, 546, A33
Tremblin P. et al., 2013, A&A, 560, A19
Urquhart J. S. et al., 2014, A&A, 568, A41
van der Tak F. F. S., Black J. H., Schöier F. L., Jansen D. J., van Dishoeck E. F., 2007, A&A, 468, 627
Walborn N. R., 1980, ApJS, 44, 535
Walborn N. R., Fitzpatrick E. L., 1990, PASP, 102, 379
White G. J. et al., 1999, A&A, 342, 233
Yamaguchi R., Saito H., Mizuno N., Mine Y., Mizuno A., Ogawa H., Fukui Y., 1999, PASJ, 51, 791

This paper has been typeset from a TEX/LATEX file prepared by the author.